JGR Space Physics

RESEARCH ARTICLE
10.1029/2022JA030969

Observations of Mercury's Plasma Sheet Horn: Characterization and Contribution to Proton Precipitation

A. N. Glass[1], J. M. Raines[1], X. Jia[1], W. Sun[1], S. Imber[2], R. M. Dewey[1], and J. A. Slavin[1]

[1]Department of Climate and Space Sciences and Engineering, University of Michigan, Ann Arbor, MI, USA, [2]Department of Physics and Astronomy, University of Leicester, Leicester, UK

Key Points:

- Mercury's northern plasma sheet horn was observed by the Fast Imaging Plasma Spectrometer and magnetometer instruments aboard Mercury Surface, Space ENvironment, GEochemistry and Ranging (MESSENGER)
- MESSENGER traversed the plasma sheet horn in three different geometries over the course of its mission at Mercury
- Proton precipitation rates in the plasma sheet horn are of the same order of magnitude as those in Mercury's dayside cusp

Correspondence to:
A. N. Glass,
anglass@umich.edu

Citation:
Glass, A. N., Raines, J. M., Jia, X., Sun, W., Imber, S., Dewey, R. M., & Slavin, J. A. (2022). Observations of Mercury's plasma sheet horn: Characterization and contribution to proton precipitation. *Journal of Geophysical Research: Space Physics*, *127*, e2022JA030969. https://doi.org/10.1029/2022JA030969

Received 1 SEP 2022
Accepted 9 DEC 2022

© 2022. American Geophysical Union. All Rights Reserved.

Abstract The Mercury Surface, Space ENvironment, GEochemistry and Ranging (MESSENGER) spacecraft was the first spacecraft to orbit the planet Mercury. Previous analysis of MESSENGER data has established that of all the planets in the solar system, Mercury's magnetosphere is the most like Earth's, dominated by the Dungey cycle in its dynamic response of the magnetosphere to solar wind forcing. In this work, we identify and describe for the first time Mercury's northern plasma sheet horn—a Dungey cycle feature key to plasma precipitation. We find three possible geometries for potential horn observation by MESSENGER and describe a case study of each. Two additional case studies are presented with geometries particularly favorable to estimating plasma precipitation within the horns. Estimates of proton precipitation flux are performed, which show precipitation levels on the order of 10^7 per cm^2 per second, on the same order of magnitude as the estimated proton precipitation flux in the dayside cusp despite the higher average energy of the protons in the horn. Potential paths for future study of the horns are discussed.

Plain Language Summary The Mercury Surface, Space ENvironment, GEochemistry and Ranging (MESSENGER) spacecraft was the first spacecraft to orbit the planet Mercury. Previous analysis of MESSENGER data has established that of all the planets in the solar system, Mercury's magnetosphere is the most like Earth's. In this work, we identify and describe for the first time Mercury's northern plasma sheet horn—a key feature present in Earth's magnetosphere which acts to guide plasma toward the surface. We find that, at Mercury, this plasma precipitates onto the planetary surface through the plasma sheet horn at a rate similar to rates previously observed for plasma precipitation on the planet's dayside. We discuss how the horn is a particularly important region for future study, because the average energy of the particles in the horn is different to particles on the dayside, and because the region of space over which the nightside precipitation happens can vary significantly.

1. Introduction

The magnetospheric dynamics of the planet Mercury are dominated by the Dungey cycle (Slavin et al., 2009). Primarily, this cycle describes the reconfiguration of magnetic fields at the dayside magnetopause as an explanation for the infiltration of the planetary magnetosphere by solar wind plasma (Dungey, 1961). This reconfiguration of fields also acts as the driver of cyclic exchange of plasma and magnetic flux between the dayside and nightside of the planetary magnetosphere. In the Dungey cycle, magnetic field lines of the solar wind reconnect with dipolar planetary field lines on the planetary dayside to create a new magnetic field topology of so-called "open" field lines, which have one footpoint within the planet and are connected through the solar wind on the other side. These contrast with "closed" field lines, which have both footpoints mapping to the planetary surface.

The convection of the solar wind away from the sun drags these newly created open field lines—and the plasma moving along them—overtop and below the planet toward the nightside. As the field lines are dragged further and further downtail, they become stretched out, and drape near each other. Like on the dayside, at some point these oppositely oriented field lines press against each other, permitting reconnection. This nightside reconnection has been observed to occur readily at Mercury (Slavin et al., 2009), as has the tailward convection of plasma along open field lines to create a "plasma mantle" (DiBraccio, Slavin, Imber, et al., 2015; DiBraccio, Slavin, Raines, et al., 2015), a feature also present at Earth. A diagram of this convection process for the solar wind is shown in Figure 1, with the path of the solar wind following the purple arrows. Magnetic field lines from Figure 1 were produced using the Block Adaptive Tree Solar-wind Roe Upwind Scheme 3D magnetohydrodynamic (MHD)

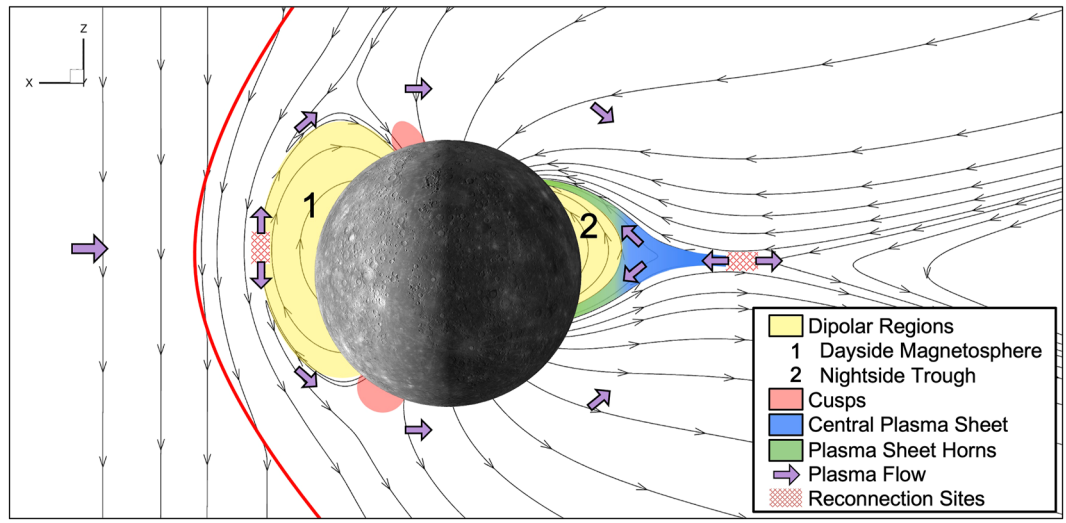

Figure 1. Diagram of the convection of solar plasma (purple) through Mercury's magnetosphere into the horns. Various regions of the magnetosphere are emphasized according to the color legend. The magnetic field lines in gray are extracted from the Block Adaptive Tree Solar-wind Roe Upwind Scheme magnetohydrodynamic model of Mercury by Jia et al. (2015).

model of Mercury (Gombosi et al., 2002; Powell et al., 1999), with a conducting core layer as presented in Jia et al. (2015).

Immediately following reconnection on the nightside the newly formed field lines are highly kinked at the reconnection site, contained within the red crossed region of Figure 1. Through a combination of the magnetic tension force and a buoyancy force, the particles running along these field lines—also referred to as "flux tubes"—are pulled toward the planet, forming a long sheet of plasma around the current sheet, called the Central Plasma Sheet (CPS) (e.g., Baumjohann et al., 1990), colored blue in Figure 1. As the particles get closer to the planet, they experience its dipole field more and more strongly, resulting in a lowering of the flux tube volume. Because of the tendency for the conservation of local specific entropy, there is a resultant increase in the local plasma pressure (Wolf et al., 2009). As the pressure grows with decreasing altitude, eventually the tension force is balanced by counteracting pressures, and the planetward flow of the ions ceases (Birn et al., 1999; Shiokawa et al., 1997). An immediate magnetic effect of this "flow braking" is compressional waves, which have been identified and investigated at Mercury (Sun, Slavin, Fu, Raines, Sundberg, et al., 2015). The CPS plasma, diverted toward higher latitudes because of this braking, forms the two "plasma sheet horns" (Suszcynsky et al., 1993), shown in green in Figure 1. Moving forward, the term CPS will exclusively refer to the downtail, non-diverted portion of the overall plasma sheet structure, and the horn will exclusively refer to the high-latitude extent of the plasma sheet. It should be noted that this division is, in theory, purely conceptual; the plasma in the horn and the plasma in the downtail CPS should be the same, even if its character in the two locations may differ, hence the gradient shading in Figure 1. The yellow region on the nightside of the planet in Figure 1, around which the horns are diverted and which CPS particles don't generally have much access to during quiet time, will be referred to herein as the "dipolar trough," owing to the low density of ions and the dominance of the planetary dipole magnetic field there.

On closed field lines, such as those that make up the horns, particles with small pitch angles occupy a region of pitch angle space which is particularly resistant to magnetic mirroring, and are therefore susceptible to loss (e.g., Sergeev & Tsyganenko, 1982). At Earth, loss of such particles to the ionosphere generates the polar aurora (Angelopoulos et al., 2008). At Mercury, which has no collisional atmosphere or ionosphere, these particles precipitate directly onto the surface; this leads to various surface interactions, including ion sputtering, which ejects neutral particles proportionally to the number of precipitating ions (Potter & Morgan, 1990). Recent studies have also shown that the neutral heavy ions that make up Mercury's exosphere may be bound to the surface more strongly than has been previously estimated (Killen et al., 2022; Morrissey et al., 2022; Szabo et al., 2018), enhancing the need to identify and constrain sources of precipitating ions with energies on the order of hundreds to thousands of electronvolts. Ion precipitation also causes electron-induced X-ray fluorescence (Starr et al., 2012), which has been previously found to be correlated on the nightside with the anticipated average location of the

open-closed field line boundary (Lindsay et al., 2016). Because of the importance of the interconnection between the plasma environment and neutral particle environment at Mercury, the dynamics of particles within the plasma sheet horns is of special relevance to a wide swath of the Mercury science community.

Some direct analysis has been performed of the plasma sheet horns at Earth (e.g., Suszcynsky et al., 1993), as well as some analysis secondary to broader studies of Earth's magnetotail (e.g., Borovsky et al., 1998). Such studies sometimes refer to the horns themselves by that name, but more commonly refer to the horns as simply the high-latitude, low-altitude extensions of the plasma sheet that lie equatorward of the tail lobes (regions bordering the magnetosheath or mantle which are mostly devoid of plasma near the planet and in which the field is stretched toward parallel with the equatorial plane) and poleward of the dipole-dominated plasmasphere. Perhaps because of interest in auroral currents, by far the greatest extent of literature describing the high-latitude plasma sheet at Earth is found within discussions of substorm dynamics. Some such studies describe the diversion of CPS plasma toward higher latitudes because of flow braking (e.g., Schödel et al., 2001), while others focus on processes at work within the horn to cause enhancement of the loss cone, and therefore of auroral precipitation (e.g., Delcourt et al., 1996). In this study, we will focus on the character the northern plasma sheet horn, which is far more likely to be observed by Mercury Surface, Space ENvironment, GEochemistry and Ranging (MESSENGER) at lower altitude, since this allows for direct study of ions impinging on the planetary surface.

Although there has not been previous work performed describing Mercury's high-latitude plasma sheet in detail, some key works provide insights important for the purposes of our analysis. The first modern analysis of Mercury's magnetotail was performed using data from the three flybys of Mercury by the MESSENGER spacecraft. This analysis established that magnetic reconnection is common on the nightside of the planet, and that the planet has a plasma sheet similar to that at the Earth (Slavin et al., 2010, 2012).

Further analysis of the planetary plasma sheet has subsequently been performed using data from the orbital phase of MESSENGER's mission, which lasted over 4,000 orbits from 2011 to 2015. Such studies have examined flux ropes (DiBraccio, Slavin, Imber, et al., 2015; DiBraccio, Slavin, Raines, et al., 2015) and dipolarization events (Dewey et al., 2017; Sun et al., 2017; Sundberg et al., 2012), and have even used MESSENGER data to deepen our understanding of flow braking and substorm currents at Mercury (Dewey et al., 2018, 2020; Poh et al., 2017, 2018). Modeling of Mercury's nightside has also been performed, including the use of MHD stress balance to discern the inner edge of the cross-tail current sheet (Poh et al., 2017), and the use of a particle-in-cell model coupled to an MHD model to investigate magnetotail asymmetries (Chen et al., 2019). However, these previous data and modeling-based studies have not explicitly addressed the magnetic or plasma environments in the plasma sheet at high latitudes.

Two works by Sun, Slavin, Fu, Raines, Zong, et al. (2015) and Sun et al. (2017), presented analysis of dynamics in the near-Mercury magnetotail, but even in instances in which a high-latitude plasma sheet is mentioned, the analysis therein is limited to plasma at low magnetic latitudes, below 20°N. The work of Rong et al. (2018) made brief mention of a bifurcated structure to the magnetotail at high latitudes close to the planet, though it did not connect this structure to plasma data in the context of the possible broader magnetic environment at Mercury. Finally, previous work by Zhao et al. (2020) provides a summary understanding of Mercury's magnetotail obtained through an average of over 4 years of MESSENGER data; however, their mission averages (most prominently displayed in Figure 3a therein) do not produce a clear picture of the average location of the high-latitude plasma sheet near the noon-midnight plane.

One prior study by Korth et al. (2014) used a magnetic field line mapping model to contextualize plasma populations throughout Mercury's near-space environment, including plasma sheet ions on the nightside. Importantly for our study, this prior study established the intuitive notion that precipitation of ions on the nightside onto the southern hemisphere, which has a weaker surface field strength, should be higher than onto the northern hemisphere. However, the tracing and mapping of plasma to invariant latitudes in that study had the side-effect of intermixing any observation of plasma in the horns with observations of plasma further downtail; the horn is therefore neither identified nor discussed therein. A later study by James et al. (2017) utilized a more developed planetary magnetic field model to trace the location of observed wave power, driven mostly by compressional waves, on the nightside of the planet; a significant portion of this power has footpoints in the portion of the nightside equatorial plane anticipated to be traversed by closed planetary field lines, that is, the plasma sheet and dipolar trough.

The recent work to model and describe observations of high-energy ions in the nightside dipolar trough by Zhao et al. (2022), which they call ring current ions, is relevant to this study because the dipolar trough is bounded by the horns. Indeed, given MESSENGER's polar orbit, observation of the dipolar trough in the noon-midnight plane necessarily implies traversal of the horns, and we will later use the findings of possible ring current ions to reinforce the likelihood of observation of the nightside dipolar trough in one of the orbits discussed in our study.

A deeper understanding of Mercury's magnetotail is valuable not just for how it informs our understanding of Mercury's magnetospheric system, but also for how it informs our understanding of plasma precipitation onto the surface as an exosphere generation mechanism. Even prior to MESSENGER's arrival at Mercury, telescope observations had already confirmed a significant density of neutral sodium in the vicinity of the planet (Potter & Killen, 2008; Potter & Morgan, 1985). Measurements from the Ultraviolet and Visible Spectrometer taken during MESSENGER's second flyby of Mercury confirmed these findings (McClintock et al., 2009).

Despite extensive study, there is not currently general agreement on the contribution of various source processes to the generation of Mercury's neutral exosphere, nor their distribution across the planetary surface. Some previous studies have shown that the predominant source region for sputtered sodium is at high latitudes, perhaps through the planetary cusps (Sarantos et al., 2001; Sun et al., 2022); although recent work has explained that a uniform exosphere could still give rise to previously observed patterns within a single hemisphere enhancement (Killen, 2020; Mangano et al., 2015). In contrast, a symmetric exosphere profile is not a sufficient explanation for asymmetric peaks of sodium regularly observed in either the northern or southern hemisphere at high latitudes (Killen, 2020); however, a single explanation for this global asymmetry has thus far eluded study, in part because the southern hemisphere surface was not well-sampled by the MESSENGER spacecraft (e.g., Peplowski et al., 2014). Because of the earlier-mentioned recent finding that sodium may be more tightly bound to the surface than previously estimated (Morrissey et al., 2022), at least one widely used model does not anticipate that a highly variable process like ion sputtering (brought about by ion precipitation) could be a dominant source process for Mercury's more slowly varying exosphere (Killen et al., 2022), and that other processes like photon-stimulated desorption (Cassidy et al., 2015) and micrometeoroid impacts (Cassidy et al., 2021; Jasinski et al., 2020) dominate. Notwithstanding that conclusion, recent analysis has also successfully shown that the cusp ion precipitation rate is well-correlated with significant variability in the density of singly ionized sodium in Mercury's near space environment (Sun et al., 2022).

In pursuit of a greater understanding of particle precipitation as it relates to the generation of the neutral and ionized heavy environment around Mercury, and to deeper connections to magnetospheric dynamics in the magnetotail previously documented in the equatorial plane, this study will supplement prior work on the horn and CPS at Earth and Mercury by providing the first detailed description of plasma in Mercury's northern plasma sheet horn, as observed by instruments aboard the MESSENGER spacecraft.

2. Methodology: Instruments and Approach

The magnetic field near the surface of the planet in the horn, lobe, and trough is dominated by the planetary dipole. This makes the horn more often clearly visible as a plasma phenomenon at high latitudes and low altitudes because it is the only one of these three regions that has a significant plasma density, and because the northern plasma mantle is not likely to be regularly observed by MESSENGER (Jasinski et al., 2017). MESSENGER's Fast Imaging Plasma Spectrometer (FIPS) has been used extensively in previous work to detect and describe key ion features of Mercury's magnetosphere, including the planetary cusp at high northern latitudes (Raines et al., 2014). FIPS was a time-of-flight mass spectrometer with sensitivity to ions with energies between 0.046 and 13.3 keV/e. FIPS had a field-of-view of 1.4 π sr, though approximately 0.25 π sr of that view was obstructed by the spacecraft, including its large sunshade (Andrews et al., 2007; Zurbuchen et al., 1998). Analysis of FIPS data is supported by examination and analysis of data collected by MESSENGER's magnetometer (MAG), which operated at its maximum time resolution of 20 samples per second of the vector magnetic field during the observations in this study (Anderson et al., 2007).

MESSENGER's orbit was highly elliptical throughout the entirety of the orbital phase with a slowly varying periapsis point above the high northern hemisphere (Moessner & McAdams, 2016). This slowly varying periapsis altitude and latitude from orbit to orbit across the mission enabled continually adjusting views of the region of space likely to be occupied by the northern horn, and the variety in sampling space allows for the possibility

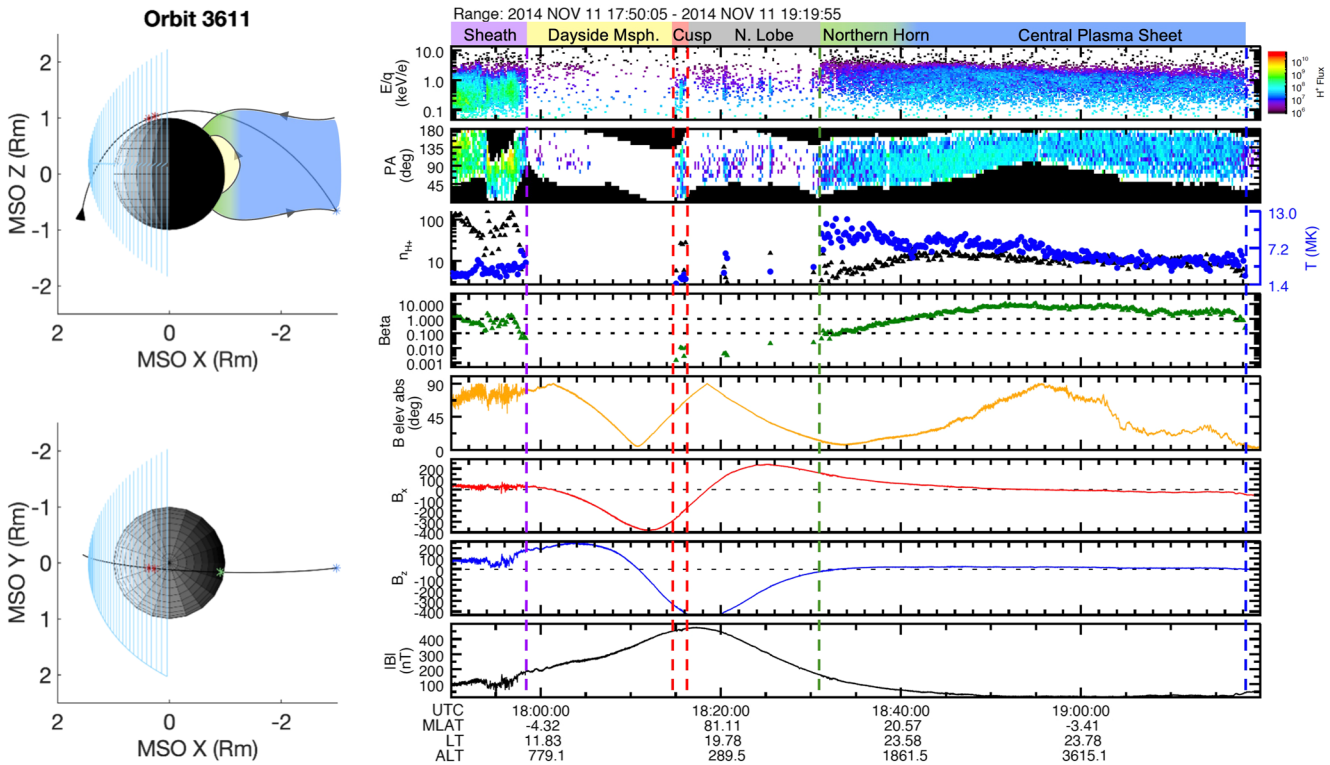

Figure 2. Continuous traversal of the northern plasma sheet horn and Central Plasma Sheet (CPS). On the right are time-series panels showing the energy spectrogram, colored according to proton flux in $(cm^2\ s\ sr\ keV)^{-1}$; pitch angle histogram; density in particles per cubic centimeter and average proton temperature; plasma beta; elevation angle of B; and the Mercury Solar Orbital (MSO) *X* and *Z* components of the magnetic field and its magnitude. Vertical lines show crossings between regions labeled across the top: the sheath, dayside magnetosphere, cusp, northern lobe, and combined northern horn—CPS structure. On the left, MESSENGER's orbit is projected into the MSO *XZ* and *XY* planes with color-coded horn and CPS and the Winslow et al. model magnetopause boundary (light blue).

that MESSENGER made a multitude of observations of the horn under various orbital geometries and magnetospheric configurations. In addition, because MESSENGER's orbit sat in a fixed plane relative to the Sun, its orbit was aligned or nearly aligned (within approximately 1 hr in either direction) with the noon-midnight plane of the planet for multiple orbits in a row, multiple times per calendar year. This enables observation in a plane of study aligned with or very near the plane in which nightside reconnection is most likely to occur. Orbits near this plane are the source of the typical horn cases identified and described herein.

3. Analysis: Case Study Examination

Given MESSENGER's orbit and the basic configuration of the CPS, plasma sheet horns, and nightside dipolar trough, we anticipate that there are three possible geometries within which FIPS would be able to observe the northern horn. First, the spacecraft could enter the northern horn and follow its arc down and away from the planet toward the CPS, passing through the embedded current sheet and then exiting the whole plasma sheet structure—we call this a "continuous traversal," owing to the continuous observation of plasma sheet plasma from high to low latitudes. Second, the spacecraft could intersect the entirety of the northern horn, crossing into the nightside dipolar trough region before passing back into either the CPS or the southern horn, depending on trajectory—we call this the "trough traversal" geometry. Finally, the spacecraft could skim the northern horn, but exit back into the northern lobe before crossing the CPS further downtail, which we call the "lobe traversal" geometry. We have selected our case study examples to showcase an observation of each of these geometries.

3.1. Continuous Traversal Geometry

Figure 2 shows the first geometry described above, of what we call a continuous traversal of the plasma sheet structure. In the top two panels of Figure 2, the time series on the right shows the FIPS measured energy

spectrogram in keV/e, and a histogram of particle pitch angle, in which black bins indicate that the pitch angle fell outside the FIPS field of view. The next two panels show bulk properties of the proton plasma—the density of protons in particles per cubic centimeter in black triangles and the average proton temperature in megakelvin in blue circles are plotted in the first panel (see Raines et al., 2011 for more detail on these calculations), and the plasma beta is plotted in the next in green triangles, and is equal to the measured plasma thermal pressure divided by the measured magnetic pressure. The next panel down shows the elevation angle as defined in the work of Imber and Slavin (2017), who investigated the extent to which field lines are stretched in the planetary lobe. An angle of 90° indicates a completely vertical field line, and a 0° elevation angle indicates that the field vector has zero relative elevation to (i.e., is complete parallel to) the equatorial plane. The next two panels show the strength (in nanotesla) of the X and Z components of the magnetic field in Mercury Solar Orbital (MSO) coordinates, in which X points directly at the Sun from the planet's center, Z points through the north pole, and Y completes the right-handed coordinate system; and the final panel shows the magnitude of the magnetic field. These time-series panels are punctuated by five colored dashed lines, demarcating times of interest.

As can be seen on the left, in the projection of this orbital extraction into the MSO X-Y and X-Z planes, the spacecraft starts its magnetospheric pass during this orbit on the dayside in the planetary magnetosheath; the dayside magnetopause surface plotted in light blue on the left is derived from the model of Winslow et al. (2013), using their best-fit parameters for the average magnetopause location ($R_{SS} = 1.45, \alpha = 0.5$). The plots on the left contain several other features to assist with interpretation. Both plots include a graphical representation of the planet, displayed as a sphere, with the lightest side facing the Sun; and colored asterisks along the black orbital trajectory of the spacecraft, corresponding to the colored demarcations in the time series panels. The top plot also contains an arrow at the start of the orbital trajectory showing the spacecraft's direction of motion; and a rough schematic sketch of the open/closed field line boundary and the boundary between the plasma sheet and the dipolar trough in gray, centered around the magnetic equatorial plane (in MSO coordinates, the $Z = 0.1989$ Rm plane; Anderson et al., 2011). Arrows on these boundaries indicate the magnetic field direction. The open/closed field line boundary is scaled to match the start and end locations of CPS observation. We have no specific knowledge of the location of the outermost field line of the dipolar trough, so its location is borrowed from orbit 203, discussed later.

Having started this magnetospheric pass moving toward the planet on the dayside, the spacecraft crosses the magnetopause on its inbound leg at the purple line in the time series. It proceeds through the dayside magnetosphere traveling upward, until it eventually crosses the planetary cusp, easily identifiable as the narrow, high-latitude, high plasma density region with similar average proton density and temperature to the equatorial magnetosheath. Continuing northward on the dayside, the spacecraft exits the cusp into the northern lobe, which is mostly devoid of plasma here, until it arrives at the region marked by the green line, at 18:31 UTC and approximately 43°N magnetic latitude on the nightside. This crossing punctuates a significant change in the character of the visible plasma.

After the green line, the proton density begins to increase significantly relative to the near-zero background of the northern lobe. Although there is significant spread in the estimated mean proton energy, it is immediately apparent that the population after the green line is far more energetic than either the sheath or the cusp. This dense, high-energy plasma population continues to be observable with nearly steady character up to the reversal of the directionality of the X component of the magnetic field at around 18:55 UTC, indicating a crossing of the nightside current sheet, and through this reversal in the southern magnetic hemisphere until the spacecraft is no longer within the structure at the blue dashed line. Given the current sheet embedded within this plasma and its near-constant character, we assert that it constitutes the full nightside plasma sheet structure. Observation of plasma sheet plasma at 43°N magnetic latitude at the beginning of this region—in other words, an extension of plasma sheet plasma at high latitude—is characteristic of the plasma sheet horn as observed at Earth.

It is unclear at what precise point the transition between the diverted plasma of the horn and the CPS occurs in this orbit; it is this very invariability that is valuable for our study. Because of the extremely short reconfiguration time of Mercury's magnetosphere of around 1–3 min (Slavin et al., 2010), the lack of variability in the plasma data and the minimal magnetic field fluctuations across the plasma sheet observation in orbit 3,611 suggests that these observations represent a steady state of the magnetosphere under some non-varying or slowly varying upstream conditions. The change to plasma beta throughout this region solidifies this assertion. The plasma beta gradually evolves from below 0.1, at the green line near the surface of the planet where the dipole field dominates, up to a steady value above 1 near the nightside current sheet. This evolution is typical of a steady-state plasma

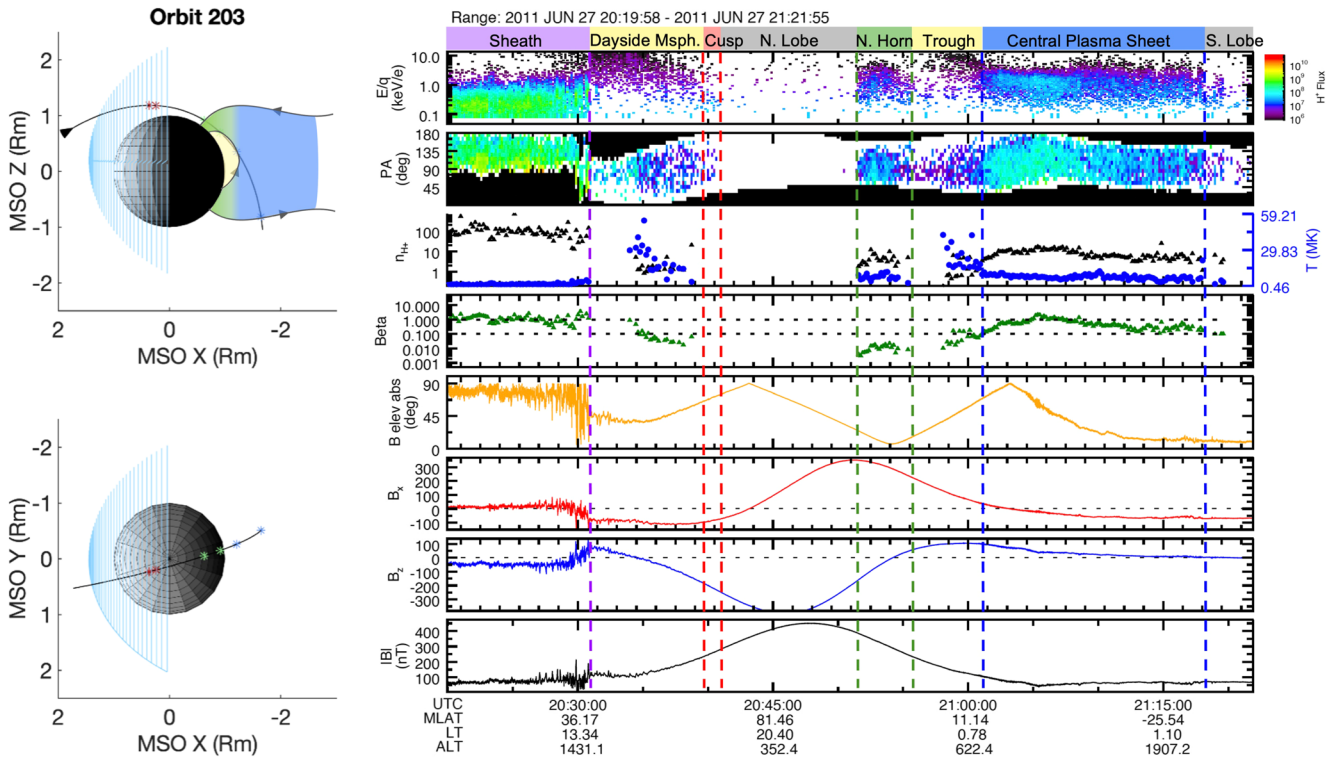

Figure 3. Trough traversal of the northern plasma sheet horn, in the style of Figure 2 except for the separated northern horn and Central Plasma Sheet regions.

sheet structure at Earth, and the lack of sharp boundaries in the plasma characteristics suggests minimal dynamics, given the short reconfiguration time of Mercury's magnetosphere. Details of the upstream conditions during this orbital pass are unfortunately unknowable, given the limitations of a single spacecraft. However, it is now possible to evaluate whether a future orbit is consistent or inconsistent with this known geometry.

3.2. Trough Traversal Geometry

With a broad intuition about the nightside under certain conditions in hand, we turn to an examination of the second of three possible geometries discussed at the outset of this section—the trough traversal, in which we believe the spacecraft passes through the horn and dipolar trough before re-entering the plasma sheet structure. Benefitting from an orbital geometry in which MESSENGER's periapsis is above the nightside of the planet, Figure 3 shows an example of such a geometry, in the style of Figure 2.

Like in orbit 3,611, MESSENGER begins this magnetosphere pass in the dayside magnetosheath. Traveling toward the planet, the spacecraft crosses over the magnetopause boundary at the purple line in the overview plot. Unlike orbit 3,611, the dayside magnetopause here does not surround a region devoid of plasma; instead, FIPS observes a significant density of plasma with energies greater than 1 keV, and with a relatively narrow pitch angle distribution centered around 90°. This observation is consistent with the ring current ions at Mercury reported by Zhao et al. (2022).

Proceeding through this population to higher latitudes, at some point MESSENGER likely skims the northern magnetospheric cusp. Identification of this region is imprecise given limited observational data, but it is also not necessary for comprehension of the nightside. For the sake of completeness, we assert that it is the span of plasma bounded by the red lines, which is sparse but appears in the energy spectrogram to have both a different character to the ring current plasma which precedes it, and a similar average energy to the magnetosheath. Exiting this region of observation of multiple plasma populations, MESSENGER enters the plasma void of the northern lobe, crossing over the dawn-dusk terminator and onto the nightside before entering the region of interest to this study. Examination of the elevation angle panel in Figure 3 suggests that the angle of the magnetic field is varying slowly and smoothly between the labeled horn and CPS on the nightside, consistent with the field there being

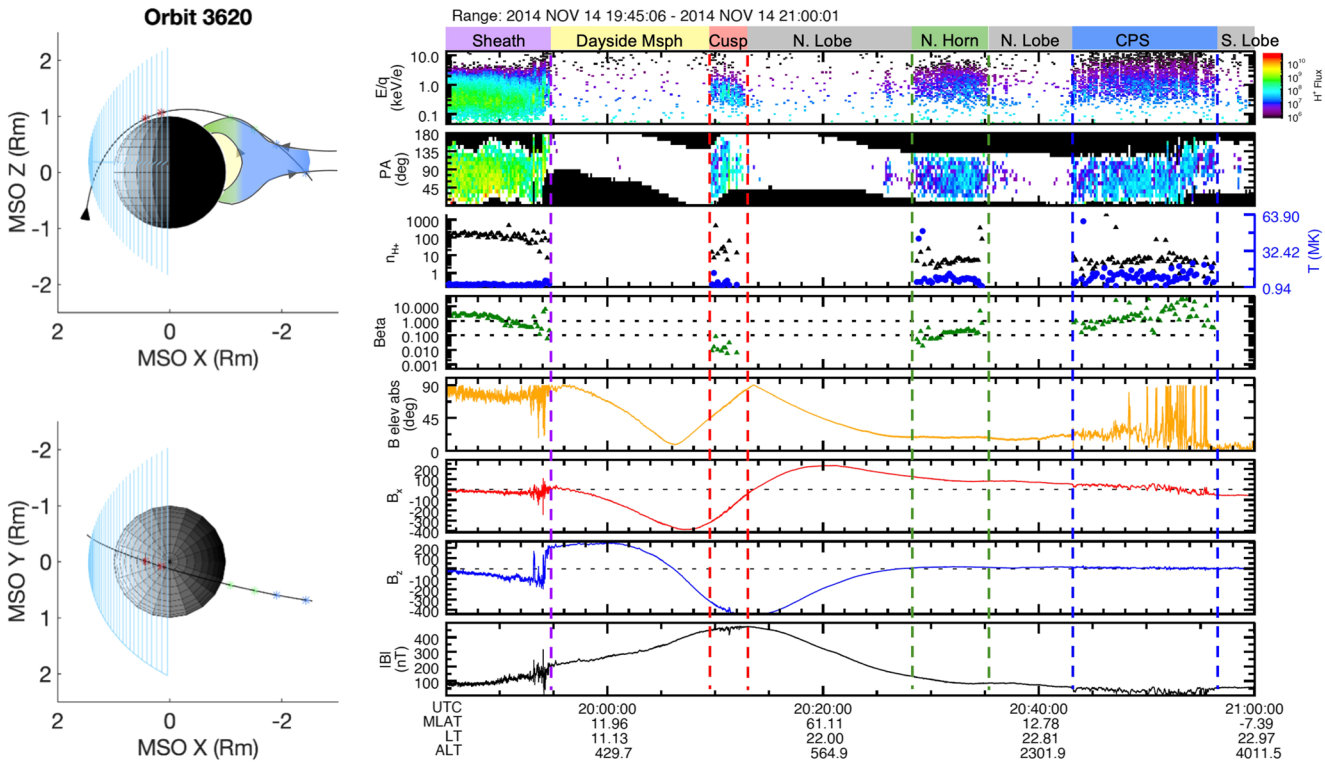

Figure 4. Lobe traversal of the northern plasma sheet horn, in the style of Figure 3.

dominated by the static dipole; a computational comparison demonstrates that the angle aligns within 2° of the expected dipolar trend. Further, we note the presence of protons with energy greater than 1 keV in the region. The presence of these particles is self-consistent with the earlier-noted observation of ring current ions in the dayside closed field region; especially considering that their pitch angle distribution is again centered around 90° and is slightly wider than the pitch angle distribution of the ring current particles on the dayside. This evolution of pitch angle distribution is consistent with both measurements and modeling reported by Zhao et al. (2022). The region between the northern enhancement and the plasma sheet, with solely high-energy plasma consistent with dayside ring current ions, and with a highly dipolar magnetic field, is the nightside dipolar trough.

Having positively identified the dipolar trough, it is certain that the northern plasma enhancement bounded by green lines is indeed the northern horn. Note that the density and mean energy of the protons in this region are less than an order of magnitude different from the density and temperature of the plasma in the CPS on average, and both are about an order of magnitude different from the ions in the sheath and ring current ions in both characteristics. This finding is consistent with the CPS and horn have the same plasma source.

3.3. Lobe Traversal Geometry

Figure 4 shows what we believe is a lobe traversal, the third and final possible geometric orientation for MESSENGER observation of the horn, in the style of Figure 3. Like orbits 203 and 3,611 the spacecraft starts its magnetospheric pass during this orbit in the dayside magnetosheath, crossing through the dayside dipolar region, the cusp, and rising over the top of the planet and then traveling downward on the nightside through the northern lobe. Like orbit 203, an enhancement of plasma at northern magnetic latitudes (here between 34°N and 20°N magnetic latitude) is present, again separated from the CPS by a region devoid of low-energy plasma.

In order to more closely examine the region devoid of low-energy plasma between the suspected horn and CPS, Figure 5 shows a detailed zoom of the elevation angle of the magnetic field in the region between the horn and CPS in orbits 203 (left) and 3,620 (right). Unlike the region determined to be the trough in orbit 203, during the traversal of the intervening region in orbit 3,620, the elevation angle of the magnetic field shows significant deviation from a simple dipole model toward 0°, indicating significant stretching of the field in the *X* and *Y*

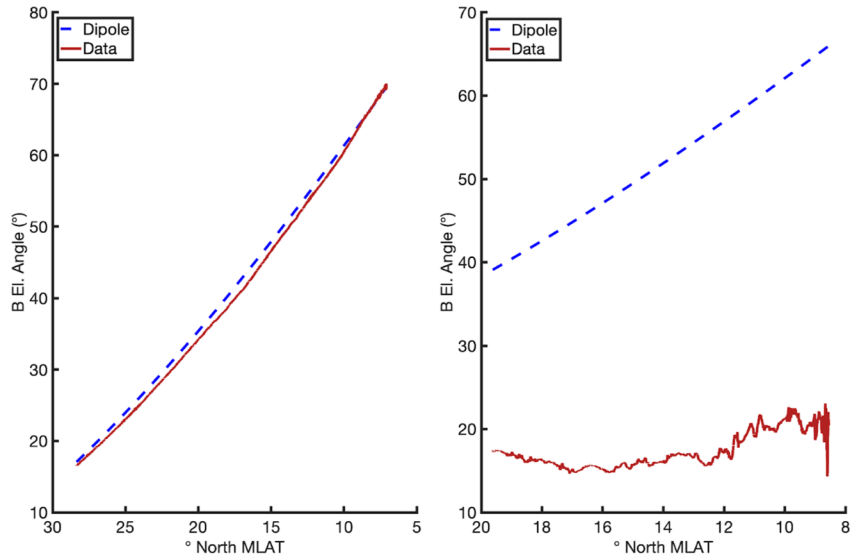

Figure 5. Measured (red solid) and dipole model (blue dashed) magnetic field elevation angle between the horn and Central Plasma Sheet in orbit 203, the trough traversal (left) and orbit 3,620, the lobe traversal (right), versus spacecraft position in magnetic latitude. We note strong agreement with the dipole model on the left; but significant stretching in the measured field on the right.

direction relative to the *Z* direction. This signature is precisely what would be expected in the mid-tail northern lobe, where field lines are highly stretched and converging toward the magnetic equator. Quantitatively, we find that the elevation angle differs from the elevation angle predicted by a dipole model by over 30° on average. This massive deviation clearly contrasts with the minimal deviation (of about 1° on average) in the dipolar trough in orbit 203. The stretched nature of the field in this region, and the lack of appreciable concurrent plasma measurement, establishes that it is the northern lobe.

Examining the average energy, density, and temperature of the northern enhancement plasma it is immediately apparent that the plasma conditions in the enhancement and the CPS are far more like each other than to any other region of the magnetosphere present. In this orbit, the proton temperature in the northern enhancement and the CPS is about an order of magnitude higher than in the sheath, and the density is about an order of magnitude lower than in the sheath; but we find again that the density and temperature in the two regions differ by less than an order of magnitude.

In contrast with the previous observation of the plasma sheet horn in the trough traversal geometry, no observation of CPS plasma is made here in which the plasma beta is far below 0.1. It is still the case that the region we assert is the horn has a lower beta than the CPS overall, like in the continuous traversal. However, it is higher on average—hovering around 0.1—than in the trough traversal case. This suggests traversal of the horn at a higher altitude than in the trough traversal case, at a relative downtail distance along the first horn field line more consistent with the continuous traversal.

Given traversal of the lobe and the horn at higher altitude, the sketch of the open-closed field line boundary in the top left of Figure 4 is adjusted relative to the previous two sketches. For this geometry and observations, a much narrower CPS is indicated, likely with a much lower downtail distance of nightside reconnection; however, analysis of these implications is beyond the scope of this study.

3.4. Single Spacecraft Limitations

One concern with MESSENGER observations, given Mercury's highly dynamic magnetosphere, is that observations of a large region in the magnetosphere may become dramatically affected by time-varying upstream conditions, muddying potential conclusions. In the case of our selections, we feel confident that this is not the case. If time-varying upstream conditions were significantly affecting the fidelity of our observations, we would expect to see strong changes in any reconnection signatures present on the nightside. For this analysis, the most accessible

of these signatures would be direct evidence of rapid changes to the plasma conditions in the plasma sheet structure, and signatures of loading or unloading in the lobe—we observe neither during any of the discussed orbits.

That said, note that we do not assert, based on only three orbits of data, that the average conditions of the magnetotail match any of the orbital observations here. Although a nearly identical tail configuration is consistent with the observations of both orbits 3,611 and 203, and inconsistent with orbit 3,620, this does not mean that either of the configurations presented is more or less likely than the other, or on average. Limited by a single spacecraft, we make no assertions at this time about the average conditions at Mercury, other than noting that the plasma sheet horns are present under some repeating configurations of the magnetosphere and are measurable under a number of orbital geometries of the MESSENGER spacecraft.

4. Results: Precipitation

Having identified the northern plasma sheet horn in data, we conclude with a first analysis of perhaps the most relevant property of the plasma sheet horn—the flux of ions contained within it that precipitate onto the planetary surface. We have identified two orbits in the very late phase of MESSENGER's mission at Mercury that are particularly well-suited for this analysis. Key characteristics of these orbits include: (a) that they are trough traversal types, permitting view of the full horn profile; (b) that FIPS's view direction is nearly anti-parallel to the magnetic field lines, allowing direct collection and analysis of ions in the precipitating population; and (c) that the spacecraft altitude within the horn is extremely low, minimizing assumption-based uncertainty in the precipitation flux calculation discussed below, and maximizing the likelihood that observed ions with very low pitch angles will indeed precipitate, without interference or unobserved dynamics.

Figure 6 shows time series panels broadly in the style of previous figures. At left, orbit 3,795 crosses through the northern horn from 36.5°N to 40.6°N magnetic latitude. The spacecraft's minimum altitude within the horn during this pass is 61 km. Orbit 3,807, the second of the two late-mission orbits, occurs only 4 Earth days later. During this orbit, the spacecraft crosses through the northern horn from 30°N to 35°N magnetic latitude, with a minimum altitude of 72 km in the horn. FIPS observed ions in the horn with pitch angles ranging from 0° to 140° in orbit 3,795, and 0° to 120° in orbit 3,807. Figure 7 shows the Energy-Resolved Pitch Angle (ERPA) diagram (in other words, panel two of Figure 6 left and right) summed across each of these two horns in time. The diagrams demonstrate FIPS' wide field of view in each of these two events, with significant coverage of the low pitch-angle (precipitating) direction.

Precipitation flux is calculated for these two horn passes in the same method as (Raines et al., 2022). First, the magnetic field as measured by the spacecraft is shifted to a surface field strength by the assumption of a dipole scaling of $1/R^3$. This assumption is particularly likely to be valid given the very low altitude of the two selected observations. Then, the components of the particle velocity parallel and perpendicular to the magnetic field are calculated. With the magnetic field and vector velocity components in hand, by application of Liouville's theorem, the observed ERPA distribution can be mapped from the spacecraft to the surface (Gershman et al., 2017). By integrating the resulting distribution from 0° to 90° (since any particle which does not have a pitch angle of at least 90° by the time it reaches the surface has not mirrored), we obtain an estimate for the precipitation flux. Using this method, the average estimated precipitation flux in orbit 3,795 is 2.9×10^7 cm^{-2}s^{-1}, and in orbit 3,807 is 4.8×10^7 cm^{-2}s^{-1}. These estimates are of the same order of magnitude as has been previously found for average proton precipitation in the northern dayside cusp (Raines et al., 2022), and about one order of magnitude less than the proton precipitation rate during active magnetopause reconnection intervals (Sun et al., 2022).

Although it is very difficult to know without an upstream monitor whether the upstream conditions for these two orbits are especially dynamic or fairly typical for Mercury, the plasma sheet during both of these orbits has a very typical character in both energy and density. Therefore, we see no reason to assume that the order of magnitude for precipitation flux estimated across these two orbits is the maximum possible in Mercury's northern horn; and given the northward offset of the dipole, the rate during these orbits should be definitionally higher in the southern horn, barring unforeseen physical processes limiting it. If they do indeed represent typical conditions, our findings here are highly consistent with the hybrid model results of Fatemi et al. (2020), who estimate a precipitation flux of around 5×10^7 cm^{-2}s^{-1} for Mercury's nightside under idealized conditions (though that model also demonstrates significant precipitation of ions at low altitudes, which we are not able to confirm through this work). As suggested by that work and now by our results, it is entirely possible that nightside precipitation is

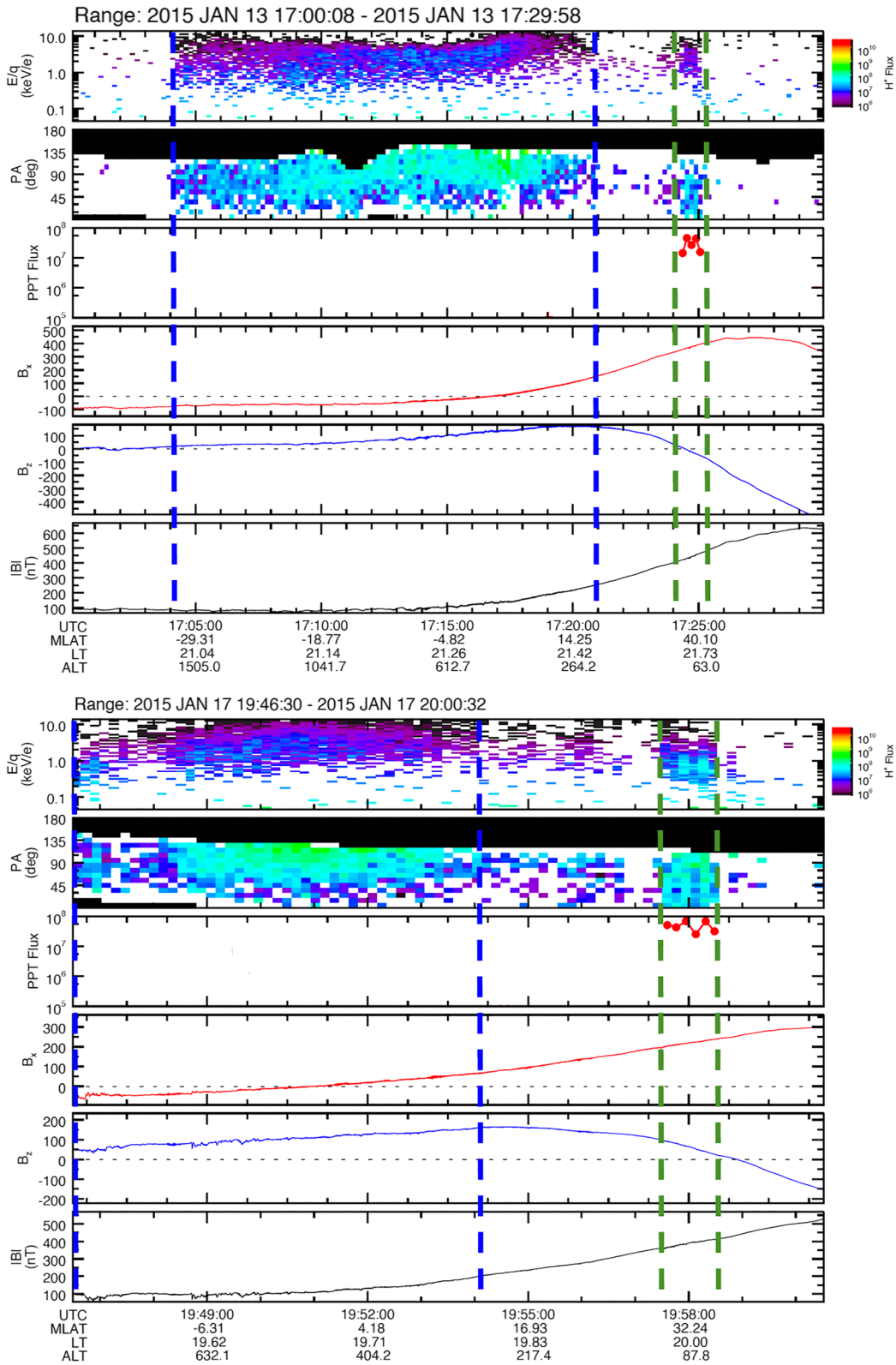

Figure 6. Two trough traversals of the northern horn with panels showing the energy spectrogram, pitch angle histogram, estimated precipitation flux (in $cm^{-2}s^{-1}$) in the horn, and the *X* and *Z* components of the magnetic field and its magnitude.

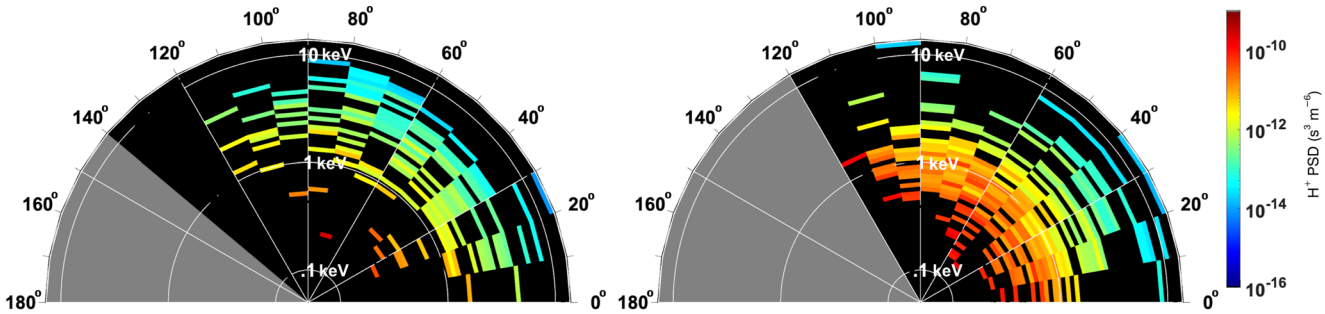

Figure 7. Summed 2D Energy-Resolved Pitch Angle diagrams for the horns during precipitation orbits, with pitch angle along the angular axis and particle energy along the radial. Both diagrams use the same colorscale for phase space, at right.

regularly as important as, or even more important than, dayside precipitation as a source of ions on the order of 1–10 keV impacting the planetary surface.

5. Conclusions and Implications for Future Work

In this study, we have for the first time identified orbital passes of the MESSENGER spacecraft in which its instruments observed the plasma sheet horn in three different geometries. Although the concept of plasma sheet horns has been previously postulated at Mercury, the separation of this concept into three theoretical geometries—and the affirmative observation of an example of each geometry—has a number of consequences for future approaches to plasma sheet analysis at Mercury, especially outside the equatorial plane.

Most fundamentally, the observation of the horns in these three different geometries suggests that MESSENGER is frequently able to observe the horn. This opens up possibilities for future work examining variable dynamics of the tail and plasma sheet, by sampling the plasma and magnetic fields connected to these regions in the horn. This is especially important because the energy spectrum of plasma sheet horn protons is broader than magnetosheath solar wind protons in the dayside cusps. While this work shows that the precipitation flux between these two regions is broadly similar, the plasma sheet horn tends to have more energetic protons, in part because protons were heated in the plasma sheet resulting in higher temperatures. Therefore, the actual effect of the precipitation on sputtering processes can be quite different between these two regions and should be the subject of future study.

Identification of the trough traversal geometry is a particularly important development from this work, as it suggests that a potentially significant portion of Mercury's nightside is protected from direct plasma precipitation at least some of the time. Affirmation of the continuous traversal geometry is also an important development for future analysis of MESSENGER data, as it affords additional opportunities for exploration of different conditions across the plasma sheet and plasma sheet horn, and for instantaneous changes in those conditions resulting from reconnection dynamics, or other dynamic processes.

We have already begun work on developing a catalog of horn observations over the entirety of MESSENGER's orbital mission at Mercury. In addition to the conclusive cases discussed in this study, we have already identified nearly 600 more examples of possible trough and lobe traversals. We will be continuing work to find additional examples of these two trajectory types, and to developing a more rigorous scheme to conclusively identify and differentiate between them. Once separated, statistical analysis of each group is possible. Analysis of a statistical set of lobe traversal geometries for horn observations affords the ability to rigorously examine downtail plasma conditions on closed field lines in the outer CPS, where features and processes at work in Earth's outer CPS and plasma sheet boundary layer may also be at play in Mercury's magnetotail. Analysis of trough traversals will permit further examination of plasma across the entire plasma sheet, permitting direct comparisons to the changing conditions across Earth's plasma sheet. Additionally, a detailed investigation of trough traversals will permit further constraining of the magnitude of plasma precipitation onto the planetary surface, including the variable area over which this precipitation happens, the variable rate of this precipitation with time, and of the extent of shielding of the planet from precipitation by the trough.

Looking beyond this catalog, and beyond MESSENGER data in general, this study's findings are also of importance for approaches to analysis of data collected on Mercury's nightside by both the Mercury Magnetospheric

Orbiter (Mio) and Mercury Planetary Orbiter (MPO) spacecraft of the BepiColombo mission, which are planned to enter orbit around Mercury in December 2025. Findings from this study suggest that, when the orbital plane of the spacecraft sits within the range of local times on the nightside over which the horn is present, MPO should observe both plasma sheet horns almost every orbit in either the trough traversal or continuous traversal orientation; and Mio might reasonably observe the plasma sheet horn in any of the three orientations presented here, depending on the local time of its periapsis. Concurrent observations of the horn at different altitudes by the two spacecraft will be particularly valuable, permitting analysis of particles along a single field line. Such observations will permit constraining uncertainty on the size of the loss cone, allowing greater precision of estimates of precipitation onto the surface. Concurrent observations of upstream conditions by Mio and the plasma sheet structure by MPO will also be valuable; especially any instances in which a change in upstream conditions rapidly propagates through Mercury's magnetosphere, altering the location of plasma sheet features and potentially even instantaneously altering the traversal geometry.

Data Availability Statement

FIPS data are publicly available for download through the NASA Planetary Data System, including through the MESSENGER EPPS repository at https://pds-ppi.igpp.ucla.edu/mission/MESSENGER/MESS/EPPS. MAG data are also available through NASA PDS, at https://pds-ppi.igpp.ucla.edu/search/?sc=Messenger&i=MAG.

Acknowledgments
This work was supported by NASA First Investigators in NASA Earth and Space Science and Technology (FINESST) Grant 80NSSC19K1526 and by NASA Discovery Data Analysis Program (DDAP) Grant 80NSSC20K1148. We also acknowledge the contributions of two anonymous reviewers, whose suggestions significantly improved the presentation of our work.

References

Anderson, B. J., Acuña, M. H., Lohr, D. A., Scheifele, J., Raval, A., Korth, H., & Slavin, J. A. (2007). The magnetometer instrument on MESSENGER. *Space Science Reviews*, *131*(1–4), 417–450. https://doi.org/10.1007/s11214-007-9246-7

Anderson, B. J., Johnson, C. L., Korth, H., Purucker, M. E., Winslow, R. M., Slavin, J. A., et al. (2011). The global magnetic field of mercury from MESSENGER orbital observations. *Science*, *333*(6051), 1859–1862. https://doi.org/10.1126/science.1211001

Andrews, G. B., Zurbuchen, T. H., Mauk, B. H., Malcom, H., Fisk, L. A., Gloeckler, G., et al. (2007). The energetic particle and plasma spectrometer instrument on the MESSENGER spacecraft. *Space Science Reviews*, *131*(1–4), 523–556. https://doi.org/10.1007/s11214-007-9272-5

Angelopoulos, V., McFadden, J. P., Larson, D., Carlson, C. W., Mende, S. B., Frey, H., et al. (2008). Tail reconnection triggering substorm onset. *Science*, *321*(5891), 931–935. https://doi.org/10.1126/science.1160495

Baumjohann, W., Paschmann, G., & Lühr, H. (1990). Characteristics of high-speed ion flows in the plasma sheet. *Journal of Geophysical Research*, *95*(A4), 3801. https://doi.org/10.1029/ja095ia04p03801

Birn, J., Hesse, M., Haerendel, G., Baumjohann, W., & Shiokawa, K. (1999). Flow braking and the substorm current wedge. *Journal of Geophysical Research*, *104*(A9), 19895–19903. https://doi.org/10.1029/1999ja900173

Borovsky, J. E., Thomsen, M. F., Elphic, R. G., Cayton, T. E., & McComas, D. J. (1998). The transport of plasma sheet material from the distant tail to geosynchronous orbit. *Journal of Geophysical Research*, *103*(A9), 20297–20331. https://doi.org/10.1029/97ja03144

Cassidy, T. A., Merkel, A. W., Burger, M. H., Sarantos, M., Killen, R. M., McClintock, W. E., & Vervack, R. J. (2015). Mercury's seasonal sodium exosphere: MESSENGER orbital observations. *Icarus*, *248*, 547–559. https://doi.org/10.1016/j.icarus.2014.10.037

Cassidy, T. A., Schmidt, C. A., Merkel, A. W., Jasinski, J. M., & Burger, M. H. (2021). Detection of large exospheric enhancements at Mercury due to meteoroid impacts. *The Planetary Science Journal*, *2*(5), 175. https://doi.org/10.3847/psj/ac1a19

Chen, Y., Tóth, G., Jia, X., Slavin, J. A., Sun, W., Markidis, S., et al. (2019). Studying dawn-dusk asymmetries of Mercury's magnetotail using MHD-EPIC simulations. *Journal of Geophysical Research: Space Physics*, *124*(11), 8954–8973. https://doi.org/10.1029/2019JA026840

Delcourt, D. C., Sauvaud, J.-A., Martin, R. F., & Moore, T. E. (1996). On the nonadiabatic precipitation of ions from the near-Earth plasma sheet. *Journal of Geophysical Research*, *101*(A8), 17409–17418. https://doi.org/10.1029/96ja01006

Dewey, R. M., Raines, J. M., Sun, W., Slavin, J. A., & Poh, G. (2018). MESSENGER observations of fast plasma flows in Mercury's magnetotail. *Geophysical Research Letters*, *45*(19), 10110–10118. https://doi.org/10.1029/2018GL079056

Dewey, R. M., Slavin, J. A., Raines, J. M., Azari, A. R., & Sun, W. (2020). MESSENGER observations of flow braking and flux pileup of dipolarizations in Mercury's magnetotail: Evidence for current wedge formation. *Journal of Geophysical Research: Space Physics*, *125*(9), e2020JA028112. https://doi.org/10.1029/2020JA028112

Dewey, R. M., Slavin, J. A., Raines, J. M., Baker, D. N., & Lawrence, D. J. (2017). Energetic electron acceleration and injection during dipolarization events in Mercury's magnetotail. *Journal of Geophysical Research: Space Physics*, *122*(12), 12170–12188. https://doi.org/10.1002/2017JA024617

DiBraccio, G. A., Slavin, J. A., Imber, S. M., Gershman, D. J., Raines, J. M., Jackman, C. M., et al. (2015). MESSENGER observations of flux ropes in Mercury's magnetotail. *Planetary and Space Science*, *115*, 77–89. https://doi.org/10.1016/j.pss.2014.12.016

DiBraccio, G. A., Slavin, J. A., Raines, J. M., Gershman, D. J., Tracy, P. J., Boardsen, S. A., et al. (2015). First observations of Mercury's plasma mantle by MESSENGER. *Geophysical Research Letters*, *42*(22), 9666–9675. https://doi.org/10.1002/2015GL065805

Dungey, J. W. (1961). Interplanetary magnetic field and the auroral zones. *Physical Review Letters*, *6*(2), 47–48. https://doi.org/10.1103/PhysRevLett.6.47

Fatemi, S., Poppe, A. R., & Barabash, S. (2020). Hybrid simulations of solar wind proton precipitation to the surface of Mercury. *Journal of Geophysical Research: Space Physics*, *125*(4), e2019JA027706. https://doi.org/10.1029/2019JA027706

Gershman, D. J., F-Viñãs, A., Dorelli, J. C., Boardsen, S. A., Avanov, L. A., Bellan, P. M., et al. (2017). Wave-particle energy exchange directly observed in a kinetic Alfvén-branch wave. *Nature Communications*, *8*(1), 14719. https://doi.org/10.1038/ncomms14719

Gombosi, T. I., Tóth, G., De Zeeuw, D. L., Hansen, K. C., Kabin, K., & Powell, K. G. (2002). Semirelativistic magnetohydrodynamics and physics-based convergence acceleration. *Journal of Computational Physics*, *177*(1), 176–205. https://doi.org/10.1006/jcph.2002.7009

Imber, S. M., & Slavin, J. A. (2017). MESSENGER observations of magnetotail loading and unloading: Implications for substorms at Mercury. *Journal of Geophysical Research: Space Physics*, *122*(11), 11402–11412. https://doi.org/10.1002/2017JA024332

James, M. K., Imber, S. M., Bunce, E. J., Yeoman, T. K., Lockwood, M., Owens, M. J., & Slavin, J. A. (2017). Interplanetary magnetic field properties and variability near Mercury's orbit. *Journal of Geophysical Research: Space Physics*, *122*(8), 7907–7924. https://doi.org/10.1002/2017JA024435

Jasinski, J. M., Regoli, L. H., Cassidy, T. A., Dewey, R. M., Raines, J. M., Slavin, J. A., et al. (2020). A transient enhancement of Mercury's exosphere at extremely high altitudes inferred from pickup ions. *Nature Communications*, *11*(1), 4350. https://doi.org/10.1038/s41467-020-18220-2

Jasinski, J. M., Slavin, J. A., Raines, J. M., & DiBraccio, G. A. (2017). Mercury's solar wind interaction as characterized by magnetospheric plasma mantle observations with MESSENGER. *Journal of Geophysical Research: Space Physics*, *122*(12), 12153–12169. https://doi.org/10.1002/2017JA024594

Jia, X., Slavin, J. A., Gombosi, T. I., Daldorff, L. K. S., Toth, G., & Van Der Holst, B. (2015). Global MHD simulations of Mercury's magnetosphere with coupled planetary interior: Induction effect of the planetary conducting core on the global interaction. *Journal of Geophysical Research: Space Physics*, *120*(6), 4763–4775. https://doi.org/10.1002/2015JA021143

Killen, R. (2020). Seeing effects on ground-based images of Mercury's sodium exosphere. In *European planetary science congress* (pp. EPSC2020–5). AA(Goddard Space Flight Center, Planetary and Geophysics Divisions). https://doi.org/10.5194/epsc2020-5

Killen, R. M., Morrissey, L. S., Burger, M. H., Vervack, R. J., Tucker, O. J., & Savin, D. W. (2022). The influence of surface binding energy on sputtering in models of the sodium exosphere of Mercury. *The Planetary Science Journal*, *3*(6), 139. https://doi.org/10.3847/psj/ac67de

Korth, H., Anderson, B. J., Gershman, D. J., Raines, J. M., Slavin, J. A., Zurbuchen, T. H., et al. (2014). Plasma distribution in Mercury's magnetosphere derived from MESSENGER magnetometer and Fast Imaging Plasma Spectrometer observations. *Journal of Geophysical Research: Space Physics*, *119*(4), 2917–2932. https://doi.org/10.1002/2013JA019567

Lindsay, S. T., James, M. K., Bunce, E. J., Imber, S. M., Korth, H., Martindale, A., & Yeoman, T. K. (2016). MESSENGER X-ray observations of magnetosphere-surface interaction on the nightside of Mercury. *Planetary and Space Science*, *125*, 72–79. https://doi.org/10.1016/j.pss.2016.03.005

Mangano, V., Massetti, S., Milillo, A., Plainaki, C., Orsini, S., Rispoli, R., & Leblanc, F. (2015). THEMIS Na exosphere observations of Mercury and their correlation with in situ magnetic field measurements by MESSENGER. *Planetary and Space Science*, *115*, 102–109. https://doi.org/10.1016/j.pss.2015.04.001

McClintock, W. E., Vervack, R. J., Bradley, E. T., Killen, R. M., Mouawad, N., Sprague, A. L., et al. (2009). MESSENGER observations of mercury's exosphere: Detection of magnesium and distribution of constituents. *Science*, *324*(5927), 610–613. https://doi.org/10.1126/science.1172525

Moessner, D. P., & McAdams, J. V. (2016). Design, implementation, and outcome of MESSENGER's trajectory from launch to mercury impact. *Advances in the Astronautical Sciences*, *156*, 3231–3250.

Morrissey, L. S., Tucker, O. J., Killen, R. M., Nakhla, S., & Savin, D. W. (2022). Solar wind ion sputtering of sodium from silicates using molecular dynamics calculations of surface binding energies. *The Astrophysical Journal Letters*, *925*(1), L6. https://doi.org/10.3847/2041-8213/ac42d8

Peplowski, P. N., Evans, L. G., Stockstill-Cahill, K. R., Lawrence, D. J., Goldsten, J. O., McCoy, T. J., et al. (2014). Enhanced sodium abundance in Mercury's north polar region revealed by the MESSENGER Gamma-Ray Spectrometer. *Icarus*, *228*, 86–95. https://doi.org/10.1016/j.icarus.2013.09.007

Poh, G., Slavin, J. A., Jia, X., Raines, J. M., Imber, S. M., Sun, W. J., et al. (2017). Mercury's cross-tail current sheet: Structure, X-line location and stress balance. *Geophysical Research Letters*, *44*(2), 678–686. https://doi.org/10.1002/2016GL071612

Poh, G., Slavin, J. A., Jia, X., Sun, W. J., Raines, J. M., Imber, S. M., et al. (2018). Transport of mass and energy in Mercury's plasma sheet. *Geophysical Research Letters*, *45*(22), 12163–12170. https://doi.org/10.1029/2018GL080601

Potter, A., & Morgan, T. (1985). Discovery of sodium in the atmosphere of Mercury. *Science*, *229*(4714), 651–653. https://doi.org/10.1126/science.229.4714.651

Potter, A. E., & Killen, R. M. (2008). Observations of the sodium tail of Mercury. *Icarus*, *194*(1), 1–12. https://doi.org/10.1016/j.icarus.2007.09.023

Potter, A. E., & Morgan, T. H. (1990). Evidence for magnetospheric effects on the sodium atmosphere of Mercury. *Science*, *248*(4957), 835–838. https://doi.org/10.1126/science.248.4957.835

Powell, K. G., Roe, P. L., Linde, T. J., Gombosi, T. I., & De Zeeuw, D. L. (1999). A solution-adaptive upwind scheme for ideal magnetohydrodynamics. *Journal of Computational Physics*, *154*(2), 284–309. https://doi.org/10.1006/jcph.1999.6299

Raines, J. M., Dewey, R. M., Staudacher, N. M., Tracy, P. J., Bert, C. M., Sarantos, M., et al. (2022). Proton precipitation in Mercury's northern magnetospheric cusp. *Journal of Geophysical Research: Space Physics*, *127*(11), e2022JA030397. https://doi.org/10.1029/2022JA030397

Raines, J. M., Gershman, D. J., Slavin, J. A., Zurbuchen, T. H., Korth, H., Anderson, B. J., & Solomon, S. C. (2014). Structure and dynamics of Mercury's magnetospheric cusp: MESSENGER measurements of protons and planetary ions. *Journal of Geophysical Research: Space Physics*, *119*(8), 6587–6602. https://doi.org/10.1002/2014ja020120

Raines, J. M., Slavin, J. A., Zurbuchen, T. H., Gloeckler, G., Anderson, B. J., Baker, D. N., et al. (2011). MESSENGER observations of the plasma environment near Mercury. *Planetary and Space Science*, *59*(15), 2004–2015. https://doi.org/10.1016/j.pss.2011.02.004

Rong, Z. J., Ding, Y., Slavin, J. A., Zhong, J., Poh, G., Sun, W. J., et al. (2018). The magnetic field structure of Mercury's magnetotail. *Journal of Geophysical Research: Space Physics*, *123*(1), 548–566. https://doi.org/10.1002/2017JA024923

Sarantos, M., Reiff, P. H., Hill, T. W., Killen, R. M., & Urquhart, A. L. (2001). A B_x-interconnected magnetosphere model for Mercury. *Planetary and Space Science*, *49*(14–15), 1629–1635. https://doi.org/10.1016/S0032-0633(01)00100-3

Schödel, R., Baumjohann, W., Nakamura, R., Sergeev, V. A., & Mukai, T. (2001). Rapid flux transport in the central plasma sheet. *Journal of Geophysical Research*, *106*(A1), 301–313. https://doi.org/10.1029/2000JA900139

Sergeev, V. A., & Tsyganenko, N. A. (1982). Energetic particle losses and trapping boundaries as deduced from calculations with a realistic magnetic field model. *Planetary and Space Science*, *30*(10), 999–1006. https://doi.org/10.1016/0032-0633(82)90149-0

Shiokawa, K., Baumjohann, W., & Haerendel, G. (1997). Braking of high-speed flows in the near-Earth tail. *Geophysical Research Letters*, *24*(10), 1179–1182. https://doi.org/10.1029/97GL01062

Slavin, J. A., Acuna, M. H., Anderson, B. J., Baker, D. N., Benna, M., Boardsen, S. A., et al. (2009). MESSENGER observations of magnetic reconnection inmercury's magnetosphere. *Science*, *324*(5927), 606–610. https://doi.org/10.1126/science.1172011

Slavin, J. A., Anderson, B. J., Baker, D. N., Benna, M., Boardsen, S. A., Gloeckler, G., et al. (2010). MESSENGER observations of extreme loading and unloading of mercury's magnetic tail. *Science*, *329*(5992), 665–668. https://doi.org/10.1126/science.1188067

Slavin, J. A., Anderson, B. J., Baker, D. N., Benna, M., Boardsen, S. A., Gold, R. E., et al. (2012). MESSENGER and Mariner 10 flyby observations of magnetotail structure and dynamics at Mercury. *Journal of Geophysical Research*, *117*(1), A00M06. https://doi.org/10.1029/2011JA016900

Starr, R. D., Schriver, D., Nittler, L. R., Weider, S. Z., Byrne, P. K., Ho, G. C., et al. (2012). MESSENGER detection of electron-induced X-ray fluorescence from Mercury's surface. *Journal of Geophysical Research*, *117*(8), E00L02. https://doi.org/10.1029/2012JE004118

Sun, W., Slavin, J. A., Milillo, A., Dewey, R. M., Orsini, S., Jia, X., et al. (2022). MESSENGER observations of planetary ion enhancements at mercury's northern magnetospheric cusp during flux transfer event showers. *Journal of Geophysical Research: Space Physics*, *127*(4), e2022JA030280. https://doi.org/10.1029/2022JA030280

Sun, W. J., Raines, J. M., Fu, S. Y., Slavin, J. A., Wei, Y., Poh, G. K., et al. (2017). MESSENGER observations of the energization and heating of protons in the near-Mercury magnetotail. *Geophysical Research Letters*, *44*(16), 8149–8158. https://doi.org/10.1002/2017GL074276

Sun, W. J., Slavin, J. A., Fu, S., Raines, J. M., Sundberg, T., Zong, Q. G., et al. (2015). MESSENGER observations of Alfvénic and compressional waves during Mercury's substorms. *Geophysical Research Letters*, *42*(15), 6189–6198. https://doi.org/10.1002/2015GL065452

Sun, W. J., Slavin, J. A., Fu, S., Raines, J. M., Zong, Q. G., Imber, S. M., et al. (2015). MESSENGER observations of magnetospheric substorm activity in Mercury's near magnetotail. *Geophysical Research Letters*, *42*(10), 3692–3699. https://doi.org/10.1002/2015GL064052

Sundberg, T., Slavin, J. A., Boardsen, S. A., Anderson, B. J., Korth, H., Ho, G. C., et al. (2012). Messenger observations of dipolarization events in Mercury's magnetotail. *Journal of Geophysical Research*, *117*(9), A00M03. https://doi.org/10.1029/2012JA017756

Suszcynsky, D. M., Gosling, J. T., & Thomsen, M. F. (1993). Ion temperature profiles in the horns of the plasma sheet. *Journal of Geophysical Research*, *98*(A1), 257–262. https://doi.org/10.1029/92ja01733

Szabo, P. S., Chiba, R., Biber, H., Stadlmayr, R., Berger, B. M., Mayer, D., et al. (2018). Solar wind sputtering of wollastonite as a lunar analogue material—Comparisons between experiments and simulations. *Icarus*, *314*, 98–105. https://doi.org/10.1016/j.icarus.2018.05.028

Winslow, R. M., Anderson, B. J., Johnson, C. L., Slavin, J. A., Korth, H., Purucker, M. E., et al. (2013). Mercury's magnetopause and bow shock from MESSENGER Magnetometer observations. *Journal of Geophysical Research: Space Physics*, *118*(5), 2213–2227. https://doi.org/10.1002/jgra.50237

Wolf, R. A., Wan, Y., Xing, X., Zhang, J. C., & Sazykin, S. (2009). Entropy and plasma sheet transport. *Journal of Geophysical Research*, *114*(5), A00D05. https://doi.org/10.1029/2009JA014044

Zhao, J. T., Zong, Q. G., Slavin, J. A., Sun, W. J., Zhou, X. Z., Yue, C., et al. (2020). Proton properties in Mercury's magnetotail: A statistical study. *Geophysical Research Letters*, *47*(19), e2020GL088075. https://doi.org/10.1029/2020GL088075

Zhao, J. T., Zong, Q. G., Yue, C., Sun, W. J., Zhang, H., Zhou, X. Z., et al. (2022). Observational evidence of ring current in the magnetosphere of Mercury. *Nature Communications*, *13*(1), 924. https://doi.org/10.1038/s41467-022-28521-3

Zurbuchen, T. H., Gloeckler, G., Cain, J. C., Lasley, S. E., & Shanks, W. (1998). Low-weight plasma instrument to be used in the inner heliosphere. In *Missions to the Sun II* (Vol. *3442*, pp. 217–224). https://doi.org/10.1117/12.330260